

Exploring the signature of two ferromagnetic states and goniopolarity in LaCrGe_3 through Hall effect

Modhumita Sariket¹, Najrul Islam¹, Saquib Shamim¹ and Nitesh Kumar^{1,*}

¹*Department of Condensed Matter and Materials Physics*

S. N. Bose National Centre for Basic Sciences, Salt Lake City, Kolkata-700106, India

LaCrGe_3 has become a playground to understand quantum critical phenomena in ferromagnetic (FM) materials. It has also garnered attention due to its peculiar two FM phases. Here, we demonstrate the presence of these phases using the Hall effect. Continuous temperature-dependent Hall resistivity measurements at fixed magnetic fields clearly demonstrate the presence of these phases, regardless of the direction of the applied magnetic field. The remanent Hall resistivity and Hall coefficient undergo a maximum and a minimum, respectively, at the boundary between the two phases. We observe a significantly large anomalous Hall conductivity of $1160 \Omega^{-1}\text{cm}^{-1}$ at 2 K when the magnetic field is applied along the magnetic easy axis, which is dominated by intrinsic effects, at least in the low-temperature FM phase. In the paramagnetic (PM) phase, hexagonal LaCrGe_3 exhibits opposite charge carrier polarities along different crystallographic directions, attributed to the anisotropic Fermi surface geometry, a phenomenon known as “goniopolarity”. The coexistence of goniopolar transport and unconventional magnetic phases may lead this material as a promising candidate for future electronic devices.

I. INTRODUCTION:

Itinerant ferromagnets are a fertile platform for exploring unconventional magnetic states where spin order emerges from the interplay between electronic correlations, crystal symmetry, and Fermi-surface topology [1]. These systems are often studied to search for novel states in the vicinity of quantum critical point [2, 3]. An itinerant ferromagnet LaCrGe_3 displays a rich temperature-pressure-magnetic field phase diagram that includes two FM phases, a tri-critical wing structure, and two antiferromagnetic (AFM) phases adjoining the PM region [4–10]. This indicates that the intricate magnetic behavior originates from the itinerant Cr $3d$ spin structure, coupled with unusual domain wall dynamics. Such domain wall dynamics can give rise to multiple ordered phases by tuning temperature alone.

LaCrGe_3 is a collinear ferromagnet with a Curie temperature $T_C=85$ K, where the existence of two distinct FM phases has been proposed [11]. The two FM (FM_1 and FM_2) phases were first assigned based on a broad maximum in the temperature derivative of the in-plane resistivity [8]. A similar behavior, indicative of two FM states, has also been reported at ambient pressure in UGe_2 based on resistivity measurements [12]. Additional experimental evidence for the presence of two FM phases in LaCrGe_3 has been provided by magnetization, resistivity, and muon spin relaxation (μSR) studies [13–15]. However, techniques such as electron spin resonance (ESR), neutron diffraction, and thermodynamic measurements have not revealed any clear signatures of two distinct FM phases [16, 17]. Beyond its ordered states, LaCrGe_3 also exhibits intriguing properties in the PM phase where NMR studies reveal spin fluctuations

with an isotropic FM character [18].

Here, we employ magneto-transport measurements in particular the Hall effect to substantiate the existence of two FM phases in LaCrGe_3 since it is highly sensitive to changes in the electronic band structure and spin-dependent scattering associated with magnetic phase transitions. Our detailed treatment of Hall effect unravels the existence of two FM phases in terms of sharp anomalies in the continuous temperature dependent Hall resistivity at fixed magnetic fields, a maximum in remanent Hall resistivity and a minimum in Hall coefficient at the boundary between two FM phases. Interestingly, we observe a so called goniopolar effect in LaCrGe_3 in the PM state by Seebeck effect combined with Hall effect studies. This hints towards a large anisotropy in the Fermi surface.

II. EXPERIMENTAL METHODS

Single crystals of LaCrGe_3 were synthesized by the self-flux method. First, a polycrystalline ingot of LaCrGe_3 was prepared by arc melting a stoichiometric amount of La (AlfaAesar, 99.9 %), Cr (Thermo Fisher, 99.99 %), and Ge (AlfaAesar, 99.9999 %). An excess of Ge was added as flux to the powdered LaCrGe_3 , with the total molar ratio maintained at 13:13:74 (La: Cr: Ge) [8]. The content was placed in an alumina crucible within a quartz tube, which was sealed under vacuum. The mixture was heated to 1100°C at a rate of 200°C for 5 hours and subsequently cooled to 825°C in 65 hours. At this temperature, excess flux was removed by centrifugation. Millimeter-sized shiny hexagonal rod-shaped single crystals were obtained. Energy-dispersive X-ray spectroscopy (EDX) data were collected to confirm the chemical composition using a field emission scanning electron microscope (Quanta 250 FEG) equipped with an Element silicon drift detector (SDD) at 25 kV accelerating

* Contact author: nitesh.kumar@bose.res.in

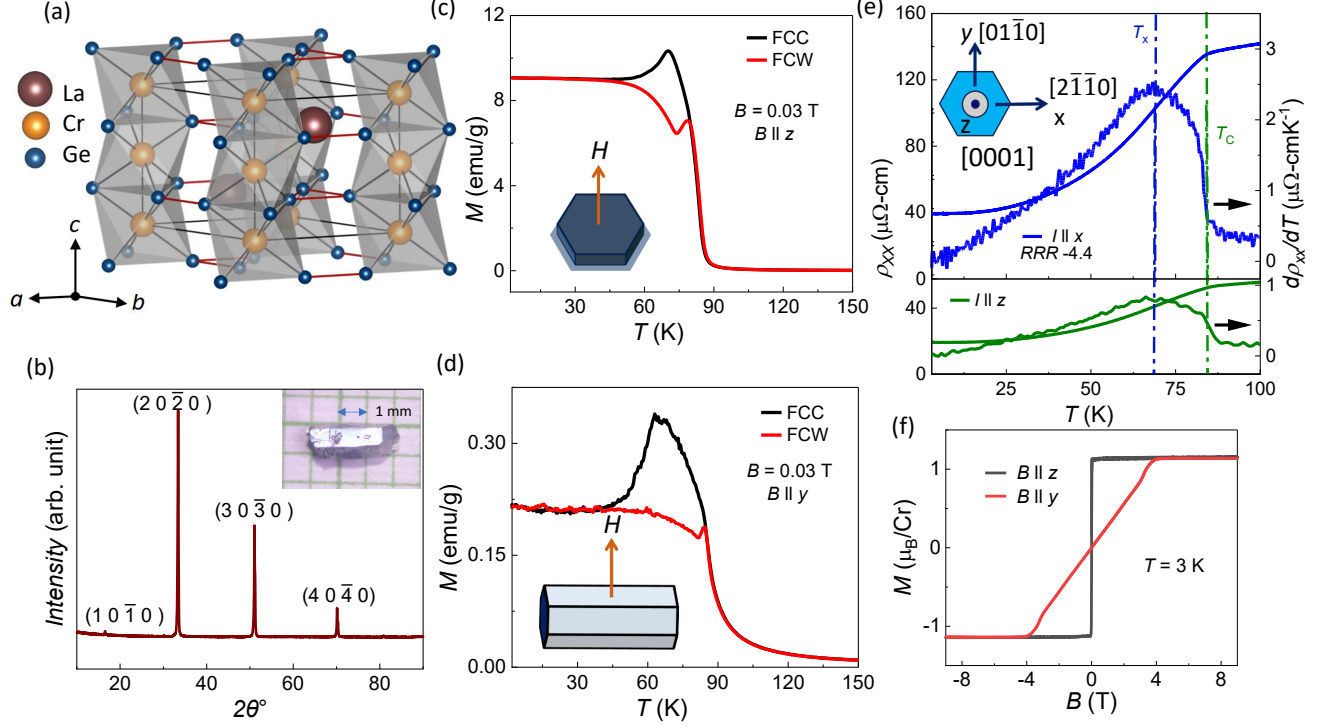


FIG. 1. (a) Crystal structure of LaCrGe_3 . (b) XRD pattern of one of the ac -planes of the single crystal which is shown in the inset. (c) and (d) Magnetic moment as a function of temperature for the measurements of field-cooled cooling (FCC) and field-cooled warming (FCW) is represented by black and red lines, respectively, while B is applied parallel to the z -axis and the y -axis. (e) Resistivity and temperature derivative of the resistivity as a function of temperature while the current is applied to the x and z axes were represented by blue and green curves, respectively. Inset represents the crystal orientations: the x -axis is along $[2\bar{1}\bar{1}0]$, y -axis along $[01\bar{1}0]$ and z -axis along $[0001]$. Green and blue lines represent the temperatures of T_C and T_x . (f) show M - B isotherms at 3 K temperature for $B||z$ and $B||y$ axes.

voltage. X-ray diffraction (XRD) of the powdered single crystals was performed at room temperature using a Rigaku SmartLab diffractometer at 9 kW with $\text{Cu K}\alpha$ radiation. XRD pattern was refined using the FullProf software. Magnetic and electrical transport measurements were performed using the VSM (Vibrating Sample Magnetometer) option and the ETO (Electrical Transport Option), respectively, in Dynacool, Physical Property Measurement System by Quantum Design, USA. Temperature-dependent magnetic measurements were performed under zero field cooling (ZFC), field cooled cooling (FCC), and field cooled warming (FCW) conditions. Magnetization loops were recorded over four quadrants, sweeping the magnetic field (B) from 9 T to -9 T. The standard four-probe method was followed to measure the longitudinal and Hall resistivity on rectangular bar-shaped crystals. Hall resistivity and longitudinal resistivity were anti-symmetrized and symmetrized, respectively, to remove the effect of probe misalignment.

The Seebeck coefficients were measured using a dipstick setup housed in a liquid nitrogen cryostat. A controlled temperature gradient was applied across rectangular bar-shaped samples, using a Keithley 2400 source measure unit. The local temperatures at the ends of the

sample were measured using PT100 sensors. The resulting thermovoltage was recorded using a high-precision nanovoltmeter (Keithley 2182A).

III. RESULT AND DISCUSSION

A. Crystal Synthesis and Characterization

LaCrGe_3 adopts a hexagonal BaNiO_3 -type crystal structure, which belongs to the space group $P6_3/mmc$. Fig. 1(a) depicts the crystal structure of LaCrGe_3 , where Cr atoms occupy the centers of face-sharing CrGe_6 octahedra [19]. These octahedra are arranged along the c -axis, forming one dimensional chains of Cr atoms with a nearest-neighbor Cr-Cr distance of approximately 2.88 Å, while the smallest Cr-Cr distance in the ab -plane is quite large (~ 6.2 Å). Each Cr atom is coordinated by Ge atoms with Cr-Ge bond lengths of around 2.52 Å. Individual chains interact through Ge forming triangular clusters with Ge-Ge distances of about ~ 2.6 Å, resulting in a breathing kagome lattice within the basal plane. La atoms occupy the space between CrGe_3 columns to make the overall three-dimensional structure of LaCrGe_3 . Fig.

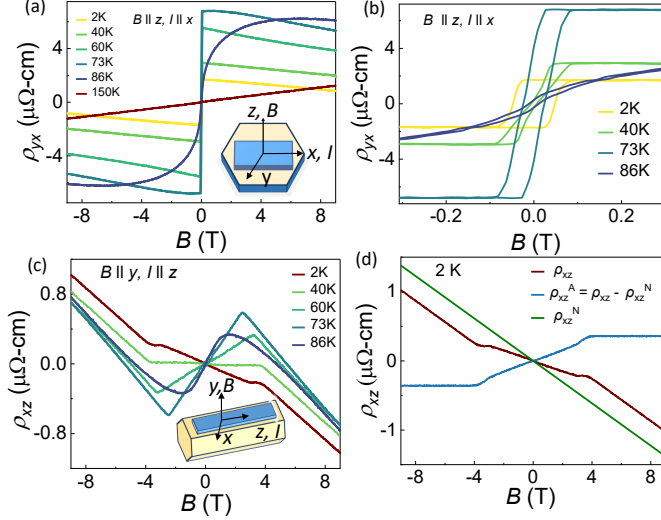


FIG. 2. (a) Field-dependent Hall resistivity, ρ_{yx} , at various temperatures, measured while sweeping B from -9 T to 9 T. The inset illustrates the magnetic field and current directions ($B||z$, $I||x$). (b) Magnified view of the low-field region of ρ_{yx} for $B||z$, $I||x$ at selected temperatures. (c) Field-dependent ρ_{xz} isotherms at different temperatures, with the inset showing the corresponding field and current directions ($B||y$, $I||z$). (d) Normal (ρ_{xz}^N) and anomalous (ρ_{xz}^A) components, along with the total Hall resistivity (ρ_{xz}), at $T = 2$ K for $B||y$, $I||z$.

1(b) shows the XRD pattern collected on a hexagonal rod-shaped crystal (inset of Fig. 1(b)) by keeping the rectangular face parallel to the sample holder. The presence of sharp peaks with only (h 0 \bar{h} 0) indices indicates that the exposed rectangular face is the ac -plane as expected. The quality as well as the orientation of the single crystal were further confirmed by Laue diffraction as shown in SI (Supplementary Information). The Rietveld refinement of the powdered single crystals is consistent with the $P6_3/mmc$ space group (see SI).

As described earlier, LaCrGe_3 is an unusual ferromagnet that not only undergoes a conventional PM to FM phase transition at $T_C=85$ K, but also exhibits an additional FM transition (T_x) at a lower temperature, indicative of a complex magnetic ordering [15] Figs. 1(c) and 1(d) show the temperature-dependent magnetization measured under FCC and FCW conditions, with an applied B of 0.03 T along the z and y axes, respectively. As the temperature is decreased there is a steep increase in the magnetization due to the ferromagnetic ordering at T_C followed by a distinct kink near 70 K in the FCC curve. The FCW curve, however, differs from the FCC curve and features an anomaly characterized by a minimum at 75 K. The magnetization curves show similar features for $B||y$ as shown in Fig. 1(d). These features have been attributed to the presence of two FM transitions corresponding to two exchange constants, in

agreement with earlier literature [20]. The decrease in magnetization in FCC below 70 K is unusual for a ferromagnet which is observed for both $B||y$ and $B||z$ directions. The discrepancy between the FCC and FCW curves can be effectively explained by the domain wall pinning-depinning mechanism [20]. Similar magnetization behavior due to domain wall pinning effect was seen in $\text{Co}_3\text{Sn}_2\text{S}_2$, Fe_3GaTe_2 [21, 22]. Temperature-dependent resistivity curves show a metallic nature with a residual resistivity ratio ($RRR = \rho_{300K}/\rho_{2K}$) value of 4.4 with a kink feature near the FM ordering temperature (Fig. 1(e)). Only in the $d\rho_{ab}/dT$, a broad maximum is seen near T_x for both the current (I) directions parallel to the x and z axes, as previously reported [8]. In Fig. 1(f), the magnetic moment saturates at a field of 0.07 T at 3 K when the field is applied parallel to the z -axis, indicating that this is the direction of easy magnetization. In contrast, for the hard direction ($B||y$ -axis), an anisotropy field of about 4 T is required to achieve the saturation magnetic moment $1.25 \mu_B/\text{Cr}$. This relatively small ordered magnetic moment compared to the effective moment in the paramagnetic (PM) state above T_C , $\mu_{eff} = 2.4 \mu_B/\text{Cr}$, indicates significant delocalization of the Cr $3d$ electrons [23].

B. Magneto-transport

To gain insight into the electrical properties of LaCrGe_3 , we performed transverse resistivity (ρ_{ij}) measurements. For a typical ferromagnet, ρ_{ij} consists of contributions from the normal Hall resistivity (ρ_{ij}^N), which arises from the magnetic Lorentz force on moving charges, and the anomalous Hall resistivity (ρ_{ij}^A) which is proportional to the sample magnetization (M) and could consist both intrinsic and extrinsic mechanisms. These contributions can be expressed through the widely used empirical formula: $\rho_{ij} = \rho_{ij}^N + \rho_{ij}^A = R_0 B + \mu_0 R_S M$, where R_0 and R_S are the ordinary Hall coefficient and the anomalous Hall coefficient, respectively, and μ_0 is the vacuum permeability [24]. ρ_{yx} as a function of B applied along the z -axis ($I||x$), is shown in Fig. 2(a). Below T_C , we find the signature of anomalous Hall effect (AHE) in terms of steep increase of Hall resistivity at low magnetic field followed by a weak linear B dependence. While the low field steep rise of Hall resistivity provides the value of anomalous Hall resistivity which has a linear magnetization dependence according to the above empirical formula, the slope in the high field region gives ordinary Hall coefficient. Above 100 K, i.e., above T_C , ρ_{yx} displays a linear field dependence in the whole field range without any slope change, characteristic of only ordinary Hall behavior. Fig. 2(b) shows the enlarged view of the data presented in Fig. 2(a) at small B and some selected temperatures in the ordered state. At 2 K, the coercive field is 0.048 T, with a remanent Hall resistivity of $1.7 \mu\Omega\text{-cm}$. Although the exact loop shape has a

weak crystal dependence, the variation of the coercive field for a fixed crystal shows a peculiar temperature dependence, which we will discuss in the next section. Fig. 2(c) shows the Hall resistivity (ρ_{xz}) for $B||y$ -axis and $I||z$ -axis at different temperatures where ρ_{xz} increases linearly and then abruptly changes the slope near 4 T. The first clear observation is that the magnitude of the slopes in the anomalous Hall and normal Hall regions are comparable. At first glance, anomalous Hall resistivity (AHR) seems to change sign from negative to positive as the temperature increases. However, when the contribution of the normal Hall effect is removed from the total Hall resistivity (see Fig. 2(d)), we recover positive AHR for all temperatures in the ordered state. The nature of the coercive field follows a similar trend with temperature as observed in the case of $B||z$ -axis as shown in the SI. For both $B||z$ and $B||y$ -axis, ρ_{ij} shows a negative

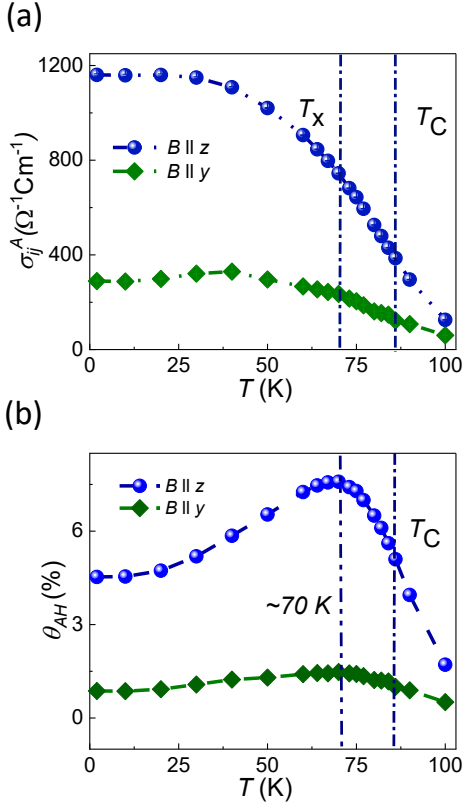


FIG. 3. (a) Anomalous Hall conductivity (σ_{ij}^A) as a function of temperature (T) for the field direction parallel to the z -axis and y -axis where two transition temperatures T_C and T_x are indicated. (b) depicts anomalous Hall angle (θ_{AH}) vs. temperature for both the directions.

slope in the high field regions below T_C , indicating the electron dominant normal electrical transport. We calculate the Hall conductivity σ_{ji} using the tensor relation, $\sigma_{ji} = \rho_{ij}/(\rho_{ij}^2 + \rho_{ii} * \rho_{jj})$. From the Hall conductivity isotherms (σ_{ij} - B data), the anomalous Hall conductiv-

ity, σ_{ji}^A , was extracted as the y -intercept of the high-field linear fit. These values are plotted as a function of temperature for both $B||y$ and $B||z$ in Fig. 3(a). At the lowest measurement temperature of 2 K, we observe $\sigma_{xz}^A = 289 \Omega^{-1}\text{cm}^{-1}$ ($B||y$) and $\sigma_{yx}^A = 1160 \Omega^{-1}\text{cm}^{-1}$ ($B||z$) which are higher than the values previously reported for the ab -plane [25]. With increasing temperature, σ_{ij}^A remains nearly constant up to 50 K, followed by a gradual decrease near T_C . The temperature-independent behavior of σ_{ij}^A for a substantial range at low temperature for both directions indicates that the anomalous Hall conductivity (AHC) is dominated by the intrinsic contribution which could have originated from the Berry curvature mechanism associated with four pairs of Weyl points observed close to the Fermi level in a recent study [25]. A detailed scaling analysis of AHE is discussed in the SI. The anomalous Hall angle (θ_{AH}) defined as $\sigma_{ij}^A/\sigma_{ij}$ (%) quantifies the relative strength of the anomalous Hall current compared to the longitudinal current [24]. We observe a significantly large θ_{AH} , reaching value as large as 7.5 % at 70 K for $B||z$ -axis. Whereas, for $B||y$ -axis, the value of θ_{AH} is relatively small (2.1 % at 70 K). For both the $B||z$ and $B||y$ axes, θ_{AH} peaks at T_x (~ 70 K) and decreases thereafter.

C. Distinguishing two FM phases

In one-dimensional systems, the nearest-neighbor distance between magnetic atoms plays a crucial role in realizing fragile magnetism. According to the Stoner model for itinerant ferromagnet LaCrGe_3 , pronounced peaks in the density of states are associated with the FM_1 and FM_2 phases [26, 27], which can also be tuned via variations in thermal parameters. Temperature-dependent XRD measurements have also previously revealed anomalies in the lattice parameters near magnetic transitions, further supporting this behavior [14]. To obtain clearer evidence of the two FM phases, we performed temperature-dependent continuous Hall resistivity measurements. For a low applied field of 0.01 T parallel to the z -axis, ρ_{yx} shows a steep increase near 85 K upon cooling, followed by a dip-like feature, and continues to decrease steadily down to the lowest measured temperature. These features correspond to two distinct transitions, at T_C and T_x , associated with the PM-FM_1 and $\text{FM}_1\text{-FM}_2$ transitions, respectively [Fig. 4(a)]. These transition temperatures shift to lower values due to the stabilization of a single-domain state as the magnetic field is increased from 0.01 T to 0.05 T and are completely suppressed above the saturation field (as seen in the curve at 5 T). From the magneto-optical Kerr effect (MOKE), two different domain structures were shown below and above 70 K temperature corresponding to two FM states [20]. Magnetoresistance ($MR = (\rho_{xx}(B) - \rho_{xx}(0))/\rho_{xx}(0)$) as a function of temperature for the applied fields of 1 T and 2 T along y -axis also reveals two transitions nearly at similar temperatures (Fig. 4(b)). In general, every

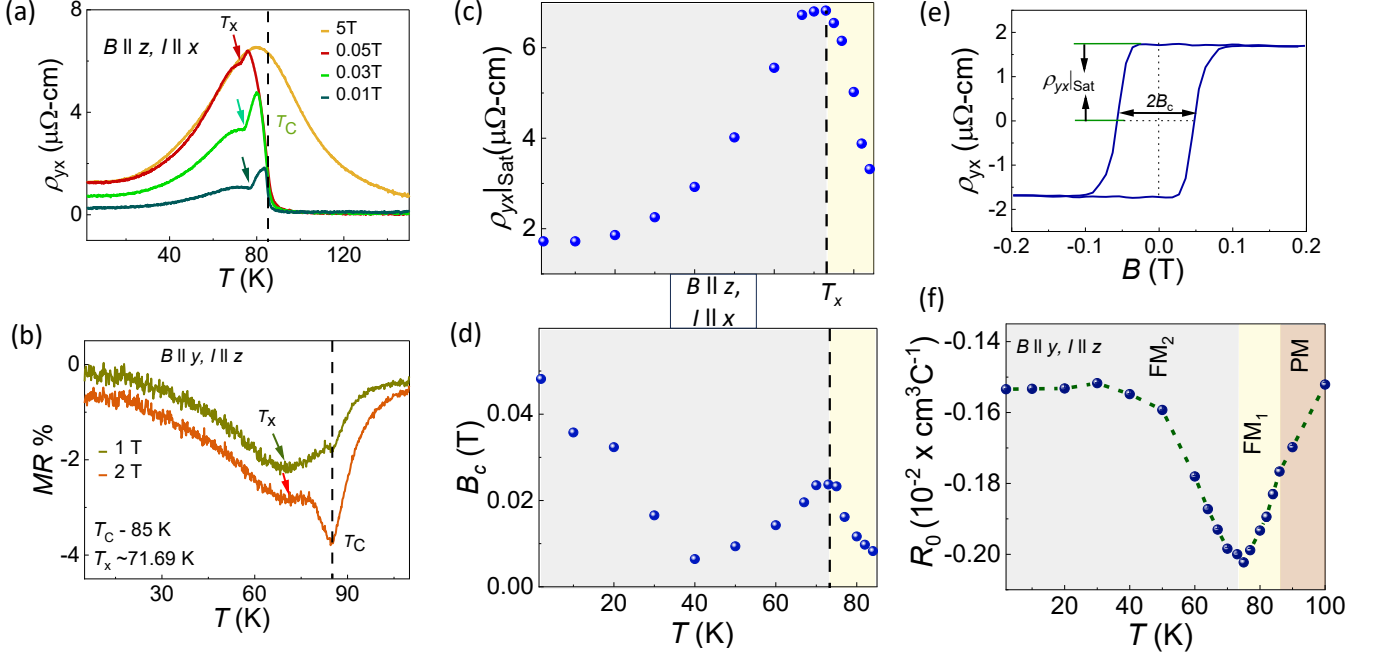


FIG. 4. (a) Hall resistivity (ρ_{yx}) as a function of temperature (T) during the heating time for the applied magnetic field 0.01 T, 0.03 T, 0.05 T and 5 T along the z -axis where T_C is PM-FM₁ and T_x is FM₁-FM₂ transitions. (b) Magneto-resistance ($MR\%$) with changing magnetic field during heating time for the applied magnetic field 1 T and 2 T the y -axis where T_C is indicated by the dashed line and T_x is indicated by the arrows. (c) and (d) $\rho_{yx}|_{sat}$ and B_c are plotted against temperature for the applied field along the z -axis where T_x is shown by a dashed line. (e) For a hysteresis loop of ρ_{yx} versus B , $\rho_{yx}|_{sat}$ and B_c are indicated. (f) Ordinary Hall coefficient is plotted against temperature for the applied field along the $B||y$ -axis where PM, FM₁ and FM₂ regions are separated by different colors.

FM system shows pinned state at very low temperature which is characterized by the largest coercivity at the lowest temperature. However, LaCrGe₃ shows another pinned state at high temperature just below T_C corresponding to FM₁ phase. Between the two pinned states, the domain-wall depinning state enhances spin-spin interactions, thereby increasing resistivity, as evidenced in the $MR\%$. From Hall resistivity against magnetic field (ρ_{yx} - B loop), we estimate coercive field (B_c), and remanent Hall resistivity $\rho_{yx}|_{sat}$, both of which peak around 73 K. In Figs. 4(c) and 4(d) FM₁-FM₂ transitions at T_x are shown from variation of $\rho_{yx}|_{sat}$ and B_c as a function of temperature. For a ρ_{yx} - B loop, $\rho_{yx}|_{sat}$ and B_c are indicated in Fig. 4(e). R_0 is calculated from the relation, $\rho_{yx}/B = R_0 + \mu_0 R_S M/B$, where R_0 is the intercept of plot ρ_{yx} vs M/B in the high field region. For $B||y$, R_0 is nearly constant below 50 K, decreases sharply up to 73 K accompanied by a slope change from negative to positive, and then increases, exhibiting a slight slope change near the FM₁-PM transition (~ 85 K). Different slopes of R_0 across FM₁-FM₂ transition may occur due to the reconstruction of the Fermi surface near the transition temperature (T_x) [28, 29]. Hence, Hall effect proves to be a potent tool to distinguish two FM phases in LaCrGe₃. PM, FM₁ and FM₂ phases are separated by different colors in the Fig. 4(f). It is important to note

that, for $B||z$, the slope of ρ_{yx} , i.e. R_0 changes its sign to positive at higher temperature in the paramagnetic region while it remains negative up to 300 K for B along y -axis [in Fig. 2(a)].

D. Signatures of Goniopolarity in Seebeck and Hall effect

The Seebeck and Hall effects are both highly sensitive to the geometry of the Fermi surface, as only the electronic states near the Fermi energy contribute significantly to transport properties. Depending on the nature of the Fermi surface, materials can show opposite charge carrier polarities along different crystallographic directions [30–45]. Such behavior can originate either from a single-band mechanism [30–33], known as goniopolarity, as observed in NaSn₂As₂ [30, 33] or from a multi-carrier mechanism [34–45], as seen in CrSb [34], where both electrons and holes from distinct bands dominate conduction along different axes. Fig. 5(a) presents the field-dependent ρ_{ij} of hexagonal LaCrGe₃ at 150 K and 200 K for both in-plane and out-of-plane Hall geometry. When the magnetic field is applied along the out-of-plane direction ($B||z$), the $\rho_{yx}(B_z)$ exhibits a positive slope, indicating dominant hole-type conduction. In con-

trast, for the in-plane direction ($B \parallel y$), the $\rho_{xz}(B_y)$ shows a negative slope, signifying dominant electron-type conduction. These observations clearly indicate the presence of direction-dependent charge carrier polarities, a hallmark of goniopolar transport [30].

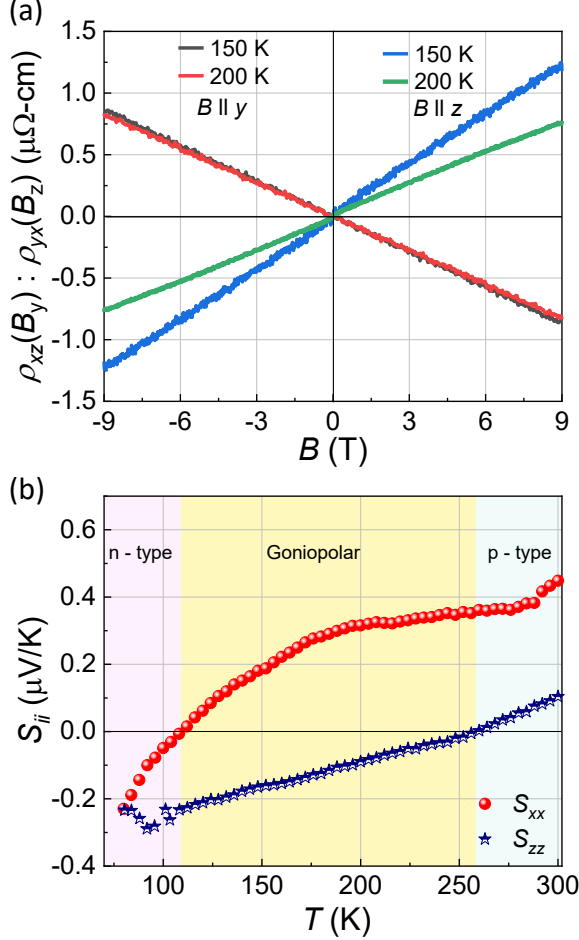


FIG. 5. (a) Magnetic field dependent Hall resistivity in-plane ($\rho_{yx}(B_z)$) and out of plane ($\rho_{xz}(B_y)$) for the temperatures 150 K and 200 K. (b) Seebeck coefficient in-plane (S_{xx}) and out of plane (S_{zz}) for the temperatures 77 K to 300 K where the n-type, goniopolar and p-type regions are indicated by different colors.

The Seebeck effect, a direct probe for determining the charge carrier type in a material, requires no application of the external magnetic field. The Seebeck coefficient (S_{ii}) is positive for hole dominant conduction and negative for electron dominant conduction. As shown in Fig. 5(b), the temperature-dependent Seebeck coefficients, measured along the in-plane (S_{xx}) and out-of-plane (S_{zz}) directions, exhibit contrasting behaviors [46]. Specifically, S_{xx} is positive above 108 K, while S_{zz} is negative below 257 K. Within this temperature range, S_{xx} and S_{zz} exhibit opposite signs, as shown in Fig. 5(b).

The Seebeck coefficient can be expressed as [30]:

$$S_{ii} = -\frac{\pi^2 k_B^2 T}{3|e|} \left[\frac{1}{n(E)} \frac{dn(E)}{dE} + \frac{1}{\tau_{ii}(E)} \frac{d\tau_{ii}}{dE} + m_{ii}^* \frac{d}{dE} \left(\frac{1}{m_{ii}^*} \right) \right]_{E=E_F} \quad (1)$$

where $n(E)$ is the energy-dependent density of states and $\tau_{ii}(E)$ is the energy-dependent scattering time. The first two terms in Eq. (1) cannot lead to a sign reversal of S_{ii} along different directions. Also the energy derivative of inverse effective mass ($m_{ii}^* \frac{d}{dE} (\frac{1}{m_{ii}^*})$) is always negative, hence the anisotropic sign of S_{ii} comes from the anisotropy in the sign of effective mass. The curvature of the electronic bands near the Fermi energy (E_F) determines the sign of m_{ii}^* . Bands with positive curvature (electron-like) yield a negative Seebeck coefficient, whereas those with negative curvature (hole-like) result in a positive Seebeck coefficient [30]. In systems with both concave and convex Fermi surface regions, such as those with hyperboloid-shaped Fermi surfaces, the sign of m_{ii}^* can vary with direction, resulting in the observed anisotropic thermoelectric behavior [46, 47].

Taken together, the Hall and Seebeck effect measurements strongly suggest that LaCrGe₃ is a goniopolar material, with direction-dependent conduction polarity arising from the anisotropic curvature of its Fermi surface. This highlights LaCrGe₃ as a promising candidate for as novel thermoelectric material for practical device applications [48, 49].

IV. SUMMARY

In this work, we have performed a detailed magneto-transport properties of the tri-critical wing compound LaCrGe₃. Hall effect measurements discern two ferromagnetic phases clearly in this compound. In the presence of small magnetic fields below the saturation field, Hall resistivity shows two distinct transitions, for PM-FM₁ and FM₁-FM₂. In addition, the temperature dependence of B_c , θ_{AH} and $\rho_{yx}|_{sat}$, R_0 provides significant changes near the transition between two ferromagnetic phases. This suggests that the electronic band structure is sensitive to such phase changes that can be detected by transport measurements. We have extended the Hall effect study in the paramagnetic region which uncovers a goniopolarity or direction-dependent conduction polarity in this compound. For a large paramagnetic temperature range, the type of majority carrier depends on the direction of the applied magnetic field, which is further supported by the Seebeck effect wherein we find opposite signs for the Seebeck coefficient for the in-plane and out-of-plane applied temperature gradient. Goniopolarity and complex magnetism coupled with peculiar domain wall dynamics make LaCrGe₃ an import candidate for future advanced electronics devices.

ACKNOWLEDGMENTS

This research was carried out using the instrumentation facilities at the Technical Research Centre (TRC), S. N. Bose National Centre for Basic Sciences, supported by the Department of Science and Technology (DST), Government of India. N.K. acknowledges financial support from the Science and Engineering Research Board

(SERB), India, under Grant No. CRG/2021/002747, as well as funding from the Max Planck Society through the Max Planck–India Partner Group program. S.S. acknowledges financial support from ANRF, SERB, India, Grant No. CRG/2023/002082. M.S. acknowledges the DST, India, for support through a fellowship. N.I. acknowledges the University Grant Commission (UGC), India, for support through a fellowship.

-
- [1] K. Buschow and F. De Boer, in *Physics of Magnetism and Magnetic Materials* (Springer, 2003) pp. 63–73.
 - [2] A. V. Chubukov, C. Pépin, and J. Rech, *Physical review letters* **92**, 147003 (2004).
 - [3] C. Huang, D. Fuchs, M. Wissinger, R. Schneider, M. Ling, M. Scheurer, J. Schmalian, and H. v. Löhneysen, *Nature communications* **6**, 8188 (2015).
 - [4] X. Lin, V. Taufour, S. L. Bud'ko, and P. C. Canfield, *Physical Review B—Condensed Matter and Materials Physics* **88**, 094405 (2013).
 - [5] V. Taufour, U. S. Kaluarachchi, S. L. Bud'ko, and P. C. Canfield, *Physica B: Condensed Matter* **536**, 483 (2018).
 - [6] E. Krenkel, M. A. Tanatar, M. Kończykowski, R. Grasset, L.-L. Wang, S. L. Bud'ko, P. C. Canfield, and R. Prozorov, *Physical Review B* **110**, 014429 (2024).
 - [7] B. Bosch-Santos, G. Cabrera-Pasca, E. Correa, B. Correa, T. Sales, K. Moon, C. Dennis, Q. Huang, J. Leao, J. Lynn, *et al.*, *Physical Review Materials* **5**, 114406 (2021).
 - [8] U. S. Kaluarachchi, S. L. Bud'ko, P. C. Canfield, and V. Taufour, *Nature communications* **8**, 546 (2017).
 - [9] D. Belitz and T. Kirkpatrick, *Physical review letters* **119**, 267202 (2017).
 - [10] V. Taufour, U. S. Kaluarachchi, R. Khasanov, M. C. Nguyen, Z. Guguchia, P. K. Biswas, P. Bonfà, R. De Renzi, X. Lin, S. K. Kim, *et al.*, *Physical review letters* **117**, 037207 (2016).
 - [11] J. Cadogan, P. Lemoine, B. R. Slater, A. Mar, and M. Avdeev, *Solid State Phenomena* **194**, 71 (2013).
 - [12] F. Hardy, C. Meingast, V. Taufour, J. Flouquet, H. v. Löhneysen, R. Fisher, N. Phillips, A. Huxley, and J. Lashley, *Physical Review B—Condensed Matter and Materials Physics* **80**, 174521 (2009).
 - [13] K. Rana, H. Kotegawa, R. Ullah, E. Gati, S. Bud'ko, P. Canfield, H. Tou, V. Taufour, and Y. Furukawa, *Physical Review B* **103**, 174426 (2021).
 - [14] E. Gati, J. M. Wilde, R. Khasanov, L. Xiang, S. Disanayake, R. Gupta, M. Matsuda, F. Ye, B. Haberl, U. Kaluarachchi, *et al.*, *Physical Review B* **103**, 075111 (2021).
 - [15] M. Xu, S. Bud'ko, R. Prozorov, and P. Canfield, *Physical Review B* **107**, 134437 (2023).
 - [16] J. Sichelschmidt, T. Gruner, D. Das, and Z. Hossain, *Journal of Physics: Condensed Matter* **33**, 495605 (2021).
 - [17] D. Das, T. Gruner, H. Pfau, U. Paramanik, U. Burkhardt, C. Geibel, and Z. Hossain, *Journal of Physics: Condensed Matter* **26**, 106001 (2014).
 - [18] K. Rana, H. Kotegawa, R. Ullah, J. Harvey, S. L. Bud'ko, P. Canfield, H. Tou, V. Taufour, and Y. Furukawa, *Physical Review B* **99**, 214417 (2019).
 - [19] H. Bie, O. Y. Zelinska, A. V. Tkachuk, and A. Mar, *Chemistry of Materials* **19**, 4613 (2007).
 - [20] R. Ullah, P. Klavins, X. Zhu, and V. Taufour, *Physical Review B* **107**, 184431 (2023).
 - [21] Z. Shen, X. Zhu, R. R. Ullah, P. Klavins, and V. Taufour, *Journal of Physics: Condensed Matter* **35**, 045802 (2022).
 - [22] M. Birch, L. Powalla, S. Wintz, O. Hovorka, K. Litzius, J. Loudon, L. Turnbull, V. Nehruji, K. Son, C. Bubeck, *et al.*, *Nature communications* **13**, 3035 (2022).
 - [23] Y. Takahashi, *Journal of the Physical Society of Japan* **55**, 3553 (1986).
 - [24] N. Nagaosa, J. Sinova, S. Onoda, A. H. MacDonald, and N. P. Ong, *Reviews of modern physics* **82**, 1539 (2010).
 - [25] L. Li, S. Guan, S. Chi, J. Li, X. Lin, G. Xu, and S. Jia, *arXiv preprint arXiv:2401.17624* (2024).
 - [26] M. C. Nguyen, V. Taufour, S. L. Bud'ko, P. C. Canfield, V. P. Antropov, C.-Z. Wang, and K.-M. Ho, *Physical Review B* **97**, 184401 (2018).
 - [27] Q. Niu, G. Knebel, D. Braithwaite, D. Aoki, G. Lapertot, M. Vališka, G. Seyfarth, W. Knafo, T. Helm, J.-P. Brison, *et al.*, *Physical Review Research* **2**, 033179 (2020).
 - [28] K. Sandeman, G. Lonzarich, and A. Schofield, *Physical review letters* **90**, 167005 (2003).
 - [29] N. Doiron-Leyraud, C. Proust, D. LeBoeuf, J. Levallois, J.-B. Bonnemaïson, R. Liang, D. Bonn, W. Hardy, and L. Taillefer, *Nature* **447**, 565 (2007).
 - [30] B. He, Y. Wang, M. Q. Arguilla, N. D. Cultrara, M. R. Scudder, J. E. Goldberger, W. Windl, and J. P. Heremans, *Nature materials* **18**, 568 (2019).
 - [31] Y. Wang, K. G. Koster, A. M. Ochs, M. R. Scudder, J. P. Heremans, W. Windl, and J. E. Goldberger, *Journal of the American Chemical Society* **142**, 2812 (2020).
 - [32] P. Yordanov, W. Sigle, P. Kaya, M. Gruner, R. Pentcheva, B. Keimer, and H.-U. Habermeier, *Physical Review Materials* **3**, 085403 (2019).
 - [33] N. Nakamura, Y. Goto, and Y. Mizuguchi, *Applied Physics Letters* **118** (2021).
 - [34] B. Rai, K. Patra, S. Bera, S. Kalimuddin, K. Deb, M. Mondal, P. Mahadevan, and N. Kumar, *Advanced Science*, 2502226 (2025).
 - [35] C. Helman, A. M. Llois, and M. Tortarolo, *Physical Review B* **104**, 195109 (2021).
 - [36] S. Luo, F. Du, D. Su, Y. Zhang, J. Zhang, J. Xu, Y. Chen, C. Cao, M. Smidman, F. Steglich, *et al.*, *Physical Review B* **108**, 195146 (2023).
 - [37] K. G. Koster, Z. Deng, C. E. Moore, J. P. Heremans, W. Windl, and J. E. Goldberger, *Chemistry of Materials* **35**, 4228 (2023).
 - [38] R. A. Nelson, Z. Deng, A. M. Ochs, K. G. Koster, C. T. Irvine, J. P. Heremans, W. Windl, and J. E. Goldberger, *Materials Horizons* **10**, 3740 (2023).

- [39] Y. Goto, H. Usui, M. Murata, J. E. Goldberger, J. P. Heremans, and C.-H. Lee, *Chemistry of Materials* **36**, 2018 (2024).
- [40] A. M. Ochs, G. H. Fecher, B. He, W. Schnelle, C. Felser, J. P. Heremans, and J. E. Goldberger, *Advanced Materials* **36**, 2308151 (2024).
- [41] V. Rowe and P. Schroeder, *Journal of Physics and Chemistry of Solids* **31**, 1 (1970).
- [42] D.-Y. Chung, T. P. Hogan, M. Rocci-Lane, P. Brazis, J. R. Ireland, C. R. Kannewurf, M. Bastea, C. Uher, and M. G. Kanatzidis, *Journal of the American Chemical Society* **126**, 6414 (2004).
- [43] C. Felser, E. Finckh, H. Kleinke, F. Rucker, and W. Tremel, *Journal of Materials Chemistry* **8**, 1787 (1998).
- [44] A. M. Ochs, P. Gorai, Y. Wang, M. R. Scudder, K. Koster, C. E. Moore, V. Stevanovic, J. P. Heremans, W. Windl, E. S. Toberer, *et al.*, *Chemistry of Materials* **33**, 946 (2021).
- [45] H. Manako, S. Ohsumi, Y. J. Sato, R. Okazaki, and D. Aoki, *Nature communications* **15**, 3907 (2024).
- [46] K. Behnia, *Fundamentals of thermoelectricity* (OUP Oxford, 2015).
- [47] J. Jan, *Helv. Phys. Acta* **41**, 957 (1968).
- [48] M. R. Scudder, B. He, Y. Wang, A. Rai, D. G. Cahill, W. Windl, J. P. Heremans, and J. E. Goldberger, *Energy & Environmental Science* **14**, 4009 (2021).
- [49] Y. Tang, B. Cui, C. Zhou, and M. Grayson, *Journal of Electronic Materials* **44**, 2095 (2015).